

Fractional quantum anomalous Hall effect in a semimetal

Wenqi Yang, Dawei Zhai, Feng-Ren Fan, and Wang Yao*

New Cornerstone Science Laboratory, Department of Physics, University of Hong Kong, Hong Kong, China

In the search of fractional quantum anomalous Hall (FQAH) effects, the conventional wisdom is to start from a flat Chern band isolated from the rest of the Hilbert space by bandgap, so that many-body interaction can be projected to a landscape that mimics a Landau level. Here we report the finding of FQAH in a 2D semimetal. Described by a 2π -flux dice lattice, the model features a flat band in touching with a dispersive lower band, where the band touching is symmetry-protected from being gapped by electron interaction. At $1/3$ and $2/3$ filling of the gapless flat band, FQAH phases are found using density matrix renormalisation group calculations taking into accounts all bands. Symmetry breaking to gap the band touching can turn the semimetal into a Chern insulator while keeping the Chern band nearly flat, but counter-intuitively this suppresses the FQAH, as the gap opening introduces strong inhomogeneity to the quantum geometry. We show an optical scheme to realize the 2π -flux dice lattice for cold atoms. Our finding uncovers a new arena for the exploration of fractional quantum Hall physics in addition to the Landau levels and Chern insulators.

Quantum anomalous Hall effects are the zero-magnetic-field analog of the quantum Hall effects, widely explored in magnetic topological insulators [1–3]. These insulators host Bloch bands of nonzero Chern number that resemble Landau levels in applied magnetic field [4], giving rise to observations of integer quantum anomalous Hall (IQAH) effects [5–8]. Besides topology, another important aspect of Landau levels is their flatness in dispersion and quantum geometry, as well as effective isolation by energy gaps. This underlies the emergence of fractional quantum Hall effects when many-body interaction projected to individual Landau level dominates the electron correlation at fractional fillings [9]. The search for *fractional quantum anomalous Hall* (FQAH) effect has therefore naturally started from insulators having a flat Chern band well isolated from all other bands by energy gaps. There has been a remarkable surge of research to engineer such flat band Chern insulators in various lattice models [10–19], where FQAH phases (or fractional Chern insulators [16]) are revealed under short-range interactions by exact diagonalization or density matrix renormalization group (DMRG) calculations. In certain models, FQAH states can exist even when the interaction strength far exceeds the band gap [20, 21]. Most notably, experimental observations of FQAH effects are recently reported in the isolated Chern band of twisted rhombohedral bilayers of MoTe_2 [22–25] and pentalayer graphene/hBN moiré [26], which are significantly advancing the research field.

In this work we report the finding of FQAH effect in the gapless flat band of a semimetal. Described by a dice lattice with a flux of 2π per cell, the model features a band touching between a flat band and a lower dispersive band, protected by a ‘dark-state symmetry’. At $\nu = 1$, i.e. dispersive (flat) band filled (empty), self-consistent Hartree phase diagram consists of two semimetal phases at weak and intermediate strengths respectively of the nearest-neighbor repulsion U_1 and a trivial insulator phase at larger U_1 . In both semimetal phases, DMRG calculations

show integer quantized charge pump characteristic of IQAH. Semimetal phase I at weak U_1 retains the symmetry protected band flatness and band touching, while semimetal II and insulating phases have spontaneous pseudospin polarization that breaks the symmetry.

Most interestingly, at $\nu = 4/3$ and $5/3$, corresponding to $1/3$ and $2/3$ fillings of the gapless flat band respectively, FQAH phases are demonstrated using real-space DMRG calculations taking into account all bands. At $\nu = 4/3$, FQAH phase is found over a small range of U_1 that falls in the semimetal I region, while at $\nu = 5/3$ FQAH phase spans over a broad range of U_1 across all three regions of the $\nu = 1$ phase diagram. In particular, due to symmetry protection on the band flatness, FQAH exists under weak interaction strength, for which a lower bound on U_1 is not observed within our computation capacity. Symmetry breaking can gap the band touching and turn the semimetal into a Chern insulator while keeping the topological band nearly flat, but counter-intuitively this tends to suppress the FQAH, as such gap opening introduces strong inhomogeneity to the otherwise nearly flat quantum geometry.

Topological properties of 2π -flux dice lattice – The lattice model concerned [Fig. 1(a)] is a variant of the tight-binding model proposed for holes in twisted rhombohedral bilayer MoTe_2 [27], consisting of three spatially separated orbitals [Fig. 1(a)]. In that context, B and C are moiré orbitals separated to opposite layers, so their mutual hopping (t') is in general much weaker compared to their hopping (t) to A orbitals that occupy both layers. The spatial variation of carriers’ layer distribution also leads to a real space Berry flux of 2π per supercell [see Fig. 1(a)]. We consider here the $t' = 0$ limit of such a flux lattice,

$$\hat{H}_0 = \sum_l E_A \hat{A}_l^\dagger \hat{A}_l - \sum_{\langle l,m \rangle} \left(t e^{i\phi_1^{l,m}} \hat{A}_l^\dagger \hat{B}_m + t e^{i\phi_2^{l,m}} \hat{A}_l^\dagger \hat{C}_m + h.c. \right), \quad (1)$$

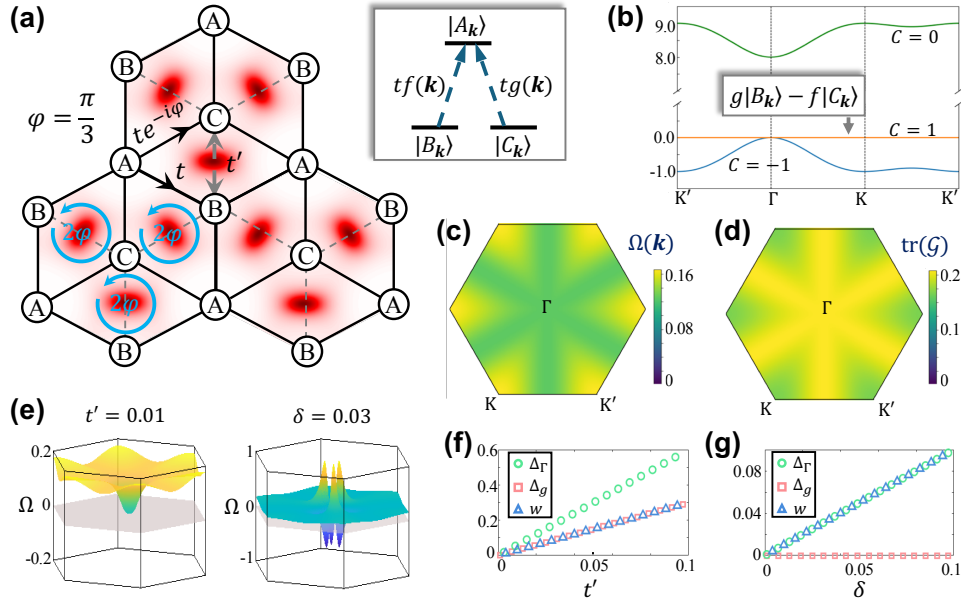


FIG. 1. **Topological properties of 2π -flux dice lattice.** (a) Schematic of the lattice, with red color in the background denoting a pseudo-magnetic field (see Fig. 4). The lattice constant is equal to 1. Inset: at an arbitrary wave vector \mathbf{k} , coupling between the three orbitals realizes a Lambda level scheme [see Eq. (2)]. (b) Band structure in non-interacting limit. The dark states of the Lambda level scheme form an exactly flat band. Its Chern number can be defined regardless of the band touching (see text). (c, d) k -space distribution of Berry curvature Ω and trace of quantum metric tensor \mathcal{G} of the flat band, respectively. (e) Berry curvature distribution in the flat band, when the band touching is gapped by a small hopping t' or energy offset δ between B and C orbitals. (f, g) Bandgap (Δ_g) between the two lower bands, their gap at Γ point (Δ_Γ), and bandwidth of the flat band (w), as functions of t' and δ . All energies here and hereafter are measured in units of the hopping amplitude t .

where the onsite energy at B and C has been set to zero, and $\langle l, m \rangle$ denote nearest-neighbors. With direct hopping between B and C vanishing, it has a bipartite geometry of a dice lattice [28, 29]. After Fourier transform, $\hat{H}_0(\mathbf{k}) = E_A \hat{A}_\mathbf{k}^\dagger \hat{A}_\mathbf{k} + t f(\mathbf{k}) \hat{A}_\mathbf{k}^\dagger \hat{B}_\mathbf{k} + t g(\mathbf{k}) \hat{A}_\mathbf{k}^\dagger \hat{C}_\mathbf{k} + h.c.$. At each wavevector \mathbf{k} , \hat{H}_0 is of a Lambda level scheme having two degenerate lower levels without direct coupling [Fig. 1(a)], which we refer as ‘dark-state symmetry’, as it allows a linear superposition $g(\mathbf{k}) \hat{B}_\mathbf{k}^\dagger - f(\mathbf{k}) \hat{C}_\mathbf{k}^\dagger$ decoupled from $\hat{A}_\mathbf{k}^\dagger$, known as the dark state in quantum optics. The coefficients

$$\begin{aligned} f(\mathbf{k}) &= -e^{i\mathbf{k}\cdot\mathbf{d}_1} - e^{-i2\pi/3} e^{i\mathbf{k}\cdot\mathbf{d}_2} - e^{i2\pi/3} e^{i\mathbf{k}\cdot\mathbf{d}_3}, \\ g(\mathbf{k}) &= e^{-i\mathbf{k}\cdot\mathbf{d}_1} + e^{-i2\pi/3} e^{-i\mathbf{k}\cdot\mathbf{d}_2} + e^{i2\pi/3} e^{-i\mathbf{k}\cdot\mathbf{d}_3}, \end{aligned} \quad (2)$$

where $\mathbf{d}_{1,2,3}$ are nearest-neighbor lattice vectors related by 120° rotations. The dark states at various \mathbf{k} form an exact flat band [Fig. 1(b)]. At the Γ point, $f(0) = g(0) = 0$, leading to the band touching with the lower dispersive band.

The Berry curvature Ω and trace of the quantum metric tensor \mathcal{G} in the flat band is smooth everywhere except at the Γ point [Fig. 1(c, d)], and the improper integral of Ω over the Brillouin zone yields a Chern number $C = \int_{\text{BZ}} \frac{d\mathbf{k}}{2\pi} \Omega(\mathbf{k}) = 1$. Likewise, the dispersive lowest band has a Chern number -1 . Their band touching point can be gapped by either adding the hopping

$t'(\hat{B}_l^\dagger \hat{C}_m + h.c.)$, or an energy offset δ between the B and C sublattices, both of which break the dark-state symmetry. For small δ and t' , the gapped bands always display the same set of Chern numbers as given above, regardless of the values of t' and δ . And in such parameter regime, the width and gaps of the flat band are linear functions of t' and δ with modest slopes [see Fig. 1(f, g)]. δ can only open a gap locally at Γ , but not a global bandgap. Notably, both terms introduce a strong inhomogeneity in the Berry curvature [Fig. 1(e) vs Fig. 1(c)].

Semimetals and IQAH at $\nu = 1$ filling – For many-body interaction, we consider here the nearest-neighbor repulsion $H_{\text{int}} = \sum_{\langle l, m \rangle} U_1^{l, m} \hat{n}_l \hat{n}_m$ of spinless fermions [see Methods]. Figure 2(a) presents the self-consistent Hartree (scHartree) phase diagram at $\nu = 1$. Phase I exists at small U_1 or small A-orbital energy E_A , where scHartree bands retain all the qualitative features of the non-interacting ones [Fig. 2(b)]. The Berry curvature distribution and Chern number in the flat band also remain identical to the non-interacting case. With the increase of U_1 , pseudospin polarization between the B and C orbitals, $p \equiv (\rho_B - \rho_C)/(\rho_B + \rho_C)$, spontaneous appears at some point, which gives rise to an effective δ that breaks the dark-state symmetry of \hat{H}_0 . Consequently, the band touching at Γ is gapped, but the global band gap remains zero and the Chern numbers unchanged [Fig. 2(c)], which characterize a semimetal phase II. Further increase of U_1

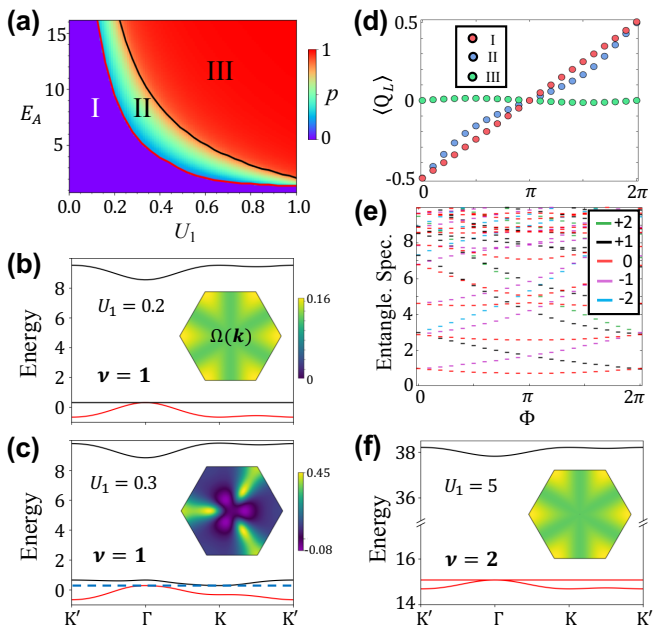


FIG. 2. **IQAH and quasiparticle bands at integer fillings.** (a) Self-consistent Hartree (scHartree) phase diagram at filling factor $\nu = 1$, consisting of two topological nontrivial semimetal phases (I and II) and a trivial insulator phase (III). Color denotes the pseudospin polarization $p = (\rho_B - \rho_C)/(\rho_B + \rho_C)$. (b, c) scHartree quasiparticle bands in semimetal phase I and II respectively. Red (black) color denotes occupied (empty) bands. (d) Examples of charge pump between the two sides of the lattice upon adiabatic change of an inserted flux Φ from DMRG calculations (see Methods), demonstrating IQAH effect in both semimetal phases I and II, and trivial insulating nature of III. Q_L is the charge polarization modulo 1 across a fixed cut in the middle. (e) Entanglement spectrum flow of state I in (d) upon the flux insertion, with different charge sectors distinguished by colors. (f) An example of scHartree bands at filling factor $\nu = 2$. The band touching and exact flatness of middle band are preserved over the entire range of U_1 explored. In (b, c, f), $E_A = 8$. The insets show the Berry curvature distribution of the middle band, which has Chern number 1 in all three cases. The Berry curvature distributions in (b) and (f) are identical to the non-interacting case in Fig. 1(c).

turns the system into a trivial insulating phase III.

The band Chern numbers in the two semimetal phases point to an unusual IQAH effect in the absence of a bandgap. This is indeed confirmed in our DMRG calculations on a cylinder geometry with periodic boundary condition along y and open boundary condition along x direction [see Methods]. Upon the adiabatic insertion of one flux quantum, an integer quantized charge pumping between the two sides of the lattice is observed in both semimetal phases I and II [Fig. 2(d)], and the entanglement spectrum is shifted by one charge sector. These are signatures of a quantized Hall conductivity of e^2/h [21, 30, 31], consistent with the Chern number -1 in the lowest scHartree band. In comparison, phase III

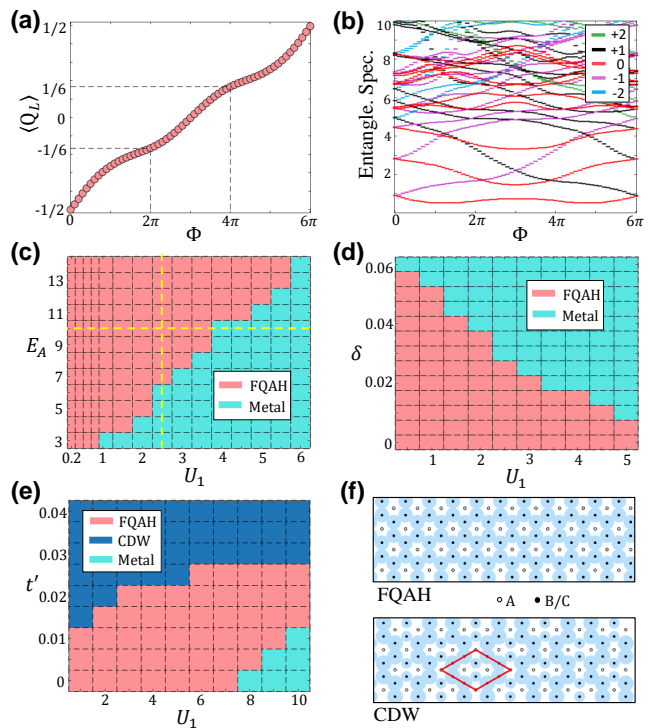


FIG. 3. **FQAH at $\nu = 5/3$ from DMRG calculations.** (a, b) Charge pumping and entanglement spectrum flow upon flux insertion. $E_A = 10$, $U_1 = 1.5$. (c) U_1 - E_A phase diagram at $t' = \delta = 0$. (d) U_1 - δ phase diagram. $t' = 0$, $E_A = 15$. (e) U_1 - t' phase diagram. $\delta = 0$, $E_A = 15$. FQAH phase, metallic phase and CDW phase are denoted by magenta, light blue and dark blue colors respectively. (f) Examples of charge distributions of FQAH phase and CDW phase. Particle populations on each orbitals are denoted by the size of the blue circles. Red diamond denotes the $\sqrt{3} \times \sqrt{3}$ supercell in the CDW state.

does not exhibit net charge pumping upon the flux insertion. From the charge pumping and the pseudospin polarization, DMRG calculations can also determine the phase diagram, which is in agreement with the scHartree diagram in Fig. 2(a) except for some quantitative differences on the phase boundaries, which can be attributed to the finite lattice size in the DMRG and the mean-field approximation in the scHartree calculations.

FQAH at $\nu = 5/3$ and $\nu = 4/3$ filling – We find FQAH phases at both these filling factors that correspond to $2/3$ and $1/3$ filling of the flat band respectively. These phases are signified by fractionally quantized charge pumping upon the adiabatic flux insertion from the DMRG calculations. Figure 3(a) presents an example of the charge pumping at $\nu = 5/3$. One charge quantum is pumped per three flux periods, signaling a fractionally quantized Hall conductivity of $e^2/(3h)$ [32]. The entanglement spectrum flow in Fig. 3(b) also provides evidence for a $1/3$ quantized charge pumping per cycle: the spectrum is shifted by one particle sector after

6π flux insertion.

Figure 3(c) presents the DMRG phase diagram at $\nu = 5/3$ in the parameter space spanned by the interaction strength U_1 and A-orbital energy E_A . It consists of the FQAH phase characterized by the $1/3$ quantized charge pumping, and a metallic phase characterized by a vanishing charge gap. Scan of the entanglement spectrum also shows a discontinuity at the phase boundary [33, 34] (c.f. Supplementary Figure S1 for the scans along the vertical and horizontal dashed lines in Fig. 3(c)). A larger E_A is favorable for stabilizing the FQAH phase in a wider range of U_1 .

We also examined the evolution of charge gap as a function of U_1 , which first increases, then decreases, reaching zero at the phase boundary and remaining vanishing in the metallic phase [see Supplementary Fig. S2 (a-c)]. The initial rise in the many-body charge gap can be attributed to the stronger interaction. After a critical U_1 within the FQAH phase, we find weak pseudospin polarization p spontaneously emerges [see Supplementary Fig. S2 (d)]. This breaks the dark-state symmetry and introduces inhomogeneity to the quantum geometry of the flat band, as already shown by the scHartree calculation at $\nu = 1$ [Fig. 2(c)]. As a result, the charge gap of the FQAH state decreases. Upon a significant increase in p [see Supplementary Fig. S2 (d)], the transition from FQAH to the metallic phase occurs, which is reminiscent of the topological transition at $\nu = 1$ from IQAH semimetal phase II to the topologically trivial phase III [Fig. 2(a)].

At $\nu = 4/3$ filling, we find FQAH phase only in a narrow region where both E_A and U_1 are small [see Supplementary Fig. S3]. It falls entirely in the region of semimetal phase I of the $\nu = 1$ diagram. Unlike the case of Fig. 3(c), at $\nu = 4/3$, a smaller E_A stabilizes the FQAH phase in a wider range of U_1 . In the FQAH phase here, two charge quanta are pumped upon 6π flux insertion, corresponding to a fractionally quantized Hall conductivity of $2e^2/(3h)$. Notably, at both $\nu = 5/3$ and $4/3$, we did not observe the lower boundary of FQAH phase as function of interaction strength U_1 within our computation capacity. The phase diagrams start from $U_1 = 0.1 - 0.2$, below which the small charge gap demands larger bond dimension for convergence.

The stark difference between the $\nu = 5/3$ and $\nu = 4/3$ FQAH phase regions, specifically in their upper boundary as function of U_1 , is not entirely unexpected. The former can be considered as $1/3$ hole added on top of $\nu = 2$ filling, while for the latter $1/3$ particle is added on top of the $\nu = 1$ filling. From the scHartree calculation, we find that at $\nu = 2$, over the entire parameter space explored in Fig. 3(c), the system retains the dark-state symmetry of \hat{H}_0 , and therefore all qualitative features of the single-particle bands, including the exact flatness of the middle band and its nearly uniform quantum geometry [Fig. 2(f)]. In contrast, at $\nu = 1$, such features are retained only in its semimetal phase I. Interaction renor-

malized quasiparticle band at the closest integer fillings indeed provides precursor for the FQAH here. Remarkably, whenever the renormalized band retains the desired dispersion and quantum geometry, the band touching is also preserved as a consequence of dark-state symmetry [Fig. 2(b, f)]. This is in contrast to the pentalayer graphene/hBN system where band touching in the single particle limit is completely lifted by Coulomb interaction at the relevant integer fillings [35–38], and a fully gapped flat Chern band then serves as the ground for FQAH.

Gapping this band touching by symmetry breaking can turn the semimetal into an insulator with nearly flat Chern band. However, this tends to quench the FQAH since the band touching is inherently associated with the uniformity of quantum geometry [39]. We demonstrate this at $\nu = 5/3$ by adding the single particle hopping t' and energy offset δ between B and C orbitals. As discussed in Fig. 1(e-g), both terms will gap the band touching point without affecting the Chern numbers, while introducing inhomogeneity to the Berry curvature.

Figure 3(d) shows the phase diagram in U_1 - δ space, fixing $E_A = 15$. Like in the $\delta = 0$ diagram in Fig. 3(c), only FQAH and metallic phases are identified within the parameter window. At larger δ , the transition from FQAH to metallic phase occurs at smaller U_1 . As onsite energy difference induces pseudospin polarization, the above trend is consistent with the observation at $\delta = 0$ where spontaneous pseudospin polarization quenches FQAH.

Figure 3(e) shows the phase diagram in U_1 - t' space at $E_A = 15$. A transition from FQAH to metallic phase at large U_1 is also observed when t' is small, as a continuation of the $t' = 0$ phase diagram. It is interesting to note that a small t' can push the FQAH to metal transition towards a larger U_1 . Additionally, increasing t' can drive a phase transition from FQAH to a $\sqrt{3} \times \sqrt{3}$ charge density wave (CDW). Figure 3(f) shows examples of the carrier distributions in FQAH and CDW phases. The CDW phase exhibits no pseudospin polarization.

Optical 2π -flux dice lattice for ultracold atoms – We generalize here the optical flux lattice scheme initially proposed by Cooper [40], for atoms of two long-lived levels moving in optical fields:

$$\hat{H} = \frac{\hat{p}^2}{2m} - \mathbf{V}(\mathbf{r}) \cdot \hat{\boldsymbol{\sigma}} = \frac{\hat{p}^2}{2m} - V(\mathbf{r})\hat{\mathbf{n}}(\mathbf{r}) \cdot \hat{\boldsymbol{\sigma}}, \quad (3)$$

where $\hat{\boldsymbol{\sigma}}$ is the vector of Pauli matrices, V and $\hat{\mathbf{n}}$ are the magnitude and direction of \mathbf{V} . The off-diagonal $V_{x,y}$ are the interspecies optical coupling generated with three travelling waves [40]: $V_x = V_0 \sum_{i=1}^3 \cos(\mathbf{g}_i \cdot \mathbf{r})$, $V_y = -V_0 \sum_{i=1}^3 \sin(\mathbf{g}_i \cdot \mathbf{r})$. V_z corresponds to a species-dependent optical potential, which we consider a form generated by three standing waves: $V_z = -V_1 \sum_{i=1}^3 \sin(\mathbf{G}_i \cdot \mathbf{r})$. The wavevectors $\mathbf{G}_1 = -(\frac{1}{\sqrt{3}}, 1) \frac{2\pi}{L}$ and $\mathbf{g}_1 = -(0, \frac{2}{3}) \frac{2\pi}{L}$ [Fig. 4(d)], and $\mathbf{G}_{2,3}$ and $\mathbf{g}_{2,3}$ are their 120° degree rotations respectively.

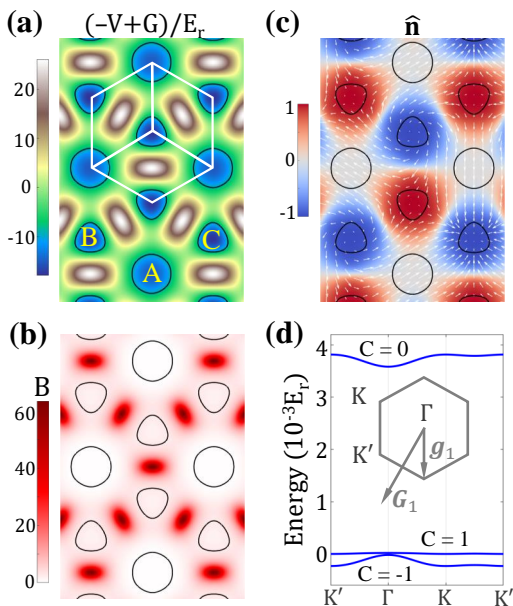


FIG. 4. 2π -flux dice lattice for ultracold atoms. (a) Potential landscape in units of $E_r = \frac{\hbar^2}{2m}|G_1|^2$. The energy has been shifted to place the barrier height between A and B/C sites at 0. (b) Pseudo-magnetic field. The flux per cell is 2π . (c) Spatial texture of $\hat{\mathbf{n}}$. Background color denotes n_z , and arrows for in-plane vector (n_x, n_y) . (d) Energy bands and Chern numbers obtained with $V_0 \approx -19.75E_r$ and $V_1 \approx -23.8E_r$. The energies have been shifted to place the flat band around zero energy.

Adiabatic motion on the local ground states with Bloch vectors along $\hat{\mathbf{n}}(\mathbf{r})$ is then governed by an effective Hamiltonian:

$$\hat{H}_{\text{adb}} = \frac{1}{2m} [\hat{\mathbf{p}} + e\mathbf{A}(\mathbf{r})]^2 - V(\mathbf{r}) + G(\mathbf{r}), \quad (4)$$

where atoms experience a periodic scalar potential with geometric correction $G = \frac{\hbar^2}{8m}(\nabla\hat{\mathbf{n}})^2$ [41], and a pseudo-magnetic field $\mathbf{B} = \nabla \times \mathbf{A} = \frac{\hbar}{2e}\hat{\mathbf{n}} \cdot (\partial_x\hat{\mathbf{n}} \times \partial_y\hat{\mathbf{n}})\mathbf{z}$. The magnetic flux threading a unit cell equals 2π , as determined by the solid angle enclosed by \mathbf{n} . For the example in Fig. 4(a-d), the three local minima in the potential landscape define the orbitals, where tunneling between the degenerate B and C sites is suppressed by a significant barrier [Fig. 4(a)], realizing a 2π flux dice lattice. The lowest three energy bands and their Chern numbers [Fig. 4(d)] indeed reproduce all features of the tight-binding Hamiltonian in Eq. (1).

Methods – DMRG calculations are performed for spinless fermions with the many-body tight-binding Hamiltonian $\hat{H} = \hat{H}_0 + \sum_{\langle l,m \rangle} U_1^{l,m} \hat{c}_m^\dagger \hat{c}_l^\dagger \hat{c}_l \hat{c}_m$ on a lattice of the cylinder geometry with open boundary condition in the x direction and periodic boundary condition in the y direction. A flux Φ threading the cylinder is introduced through the twisted boundary condition [32]. The total number of lattice sites $N = N_y \times N_x \times 3$, $N_y = 4$ and

$N_x = 24$ being the number of unit cells in the y and x directions. We have checked convergence by confirming that larger values of bond dimension D give identical results. Calculations at integer filling used bond dimensions up to $D = 256$. At $\nu = 5/3$ filling, a maximal bond dimension of $D = 300$ is used. At $\nu = 4/3$ filling, the maximal $D = 500$ due to the smaller charge gap. The DMRG simulation is performed using the ITensor library with $U(1)$ symmetry [42].

Self-consistent Hartree calculations at integer fillings are performed with the mean-field Hamiltonian: $\hat{H} = \hat{H}_0 + \sum_{\langle l,m \rangle} U_1^{l,m} \langle \hat{c}_m^\dagger \hat{c}_m \rangle \hat{c}_l^\dagger \hat{c}_l$, where the Hartree potential in the second term is determined from the wavefunctions. By comparing the total energies of solutions with different site-occupation configurations, ground states are obtained.

In the calculations, nearest-neighbor repulsion between B and C orbitals is set slightly different ($0.9U_1$) from their repulsion with A orbital (U_1), to reflect the different nature of these orbitals, whereas the choice only have minor quantitative effect on the phase boundaries.

Acknowledgment – We thank Bin-Bin Chen, Wei Zheng, Zhen Zheng, Zuzhang Lin, Jie Wang and Qian Niu for helpful discussions. Wenqi Yang thanks Tao Xiang, Kang Wang and Runze Chi for guidance on learning DMRG. The work is supported by Research Grant Council of Hong Kong SAR (HKU SFRFS2122-7S05, AoE/P-701/20, A-HKU705/21), and New Cornerstone Science Foundation.

* wangyao@hku.hk

- [1] F. D. M. Haldane, *Phys. Rev. Lett.* **61**, 2015 (1988).
- [2] Y. Tokura, K. Yasuda, and A. Tsukazaki, *Nat. Rev. Phys.* **1**, 126 (2019).
- [3] C.-Z. Chang, C.-X. Liu, and A. H. MacDonald, *Rev. Mod. Phys.* **95**, 011002 (2023).
- [4] D. J. Thouless, M. Kohmoto, M. P. Nightingale, and M. den Nijs, *Phys. Rev. Lett.* **49**, 405 (1982).
- [5] C.-Z. Chang, J. Zhang, X. Feng, J. Shen, Z. Zhang, M. Guo, K. Li, Y. Ou, P. Wei, L.-L. Wang, *et al.*, *Science* **340**, 167 (2013).
- [6] Y. Deng, Y. Yu, M. Z. Shi, Z. Guo, Z. Xu, J. Wang, X. H. Chen, and Y. Zhang, *Science* **367**, 895 (2020).
- [7] M. Serlin, C. L. Tschirhart, H. Polshyn, Y. Zhang, J. Zhu, K. Watanabe, T. Taniguchi, L. Balents, and A. F. Young, *Science* **367**, 900 (2020).
- [8] T. Li, S. Jiang, B. Shen, Y. Zhang, L. Li, Z. Tao, T. Devakul, K. Watanabe, T. Taniguchi, L. Fu, J. Shan, and K. F. Mak, *Nature* **600**, 641 (2021).
- [9] B. I. Halperin and J. K. Jain, *Fractional quantum Hall effects: new developments* (World Scientific, Singapore, 2020).
- [10] E. Tang, J.-W. Mei, and X.-G. Wen, *Phys. Rev. Lett.* **106**, 236802 (2011).
- [11] Y.-L. Wu, B. A. Bernevig, and N. Regnault, *Phys. Rev. B* **85**, 075116 (2012).

- [12] K. Sun, Z. Gu, H. Katsura, and S. D. Sarma, *Phys. Rev. Lett.* **106**, 236803 (2011).
- [13] T. Neupert, L. Santos, C. Chamon, and C. Mudry, *Phys. Rev. Lett.* **106**, 236804 (2011).
- [14] D. Sheng, Z.-C. Gu, K. Sun, and L. Sheng, *Nat. Commun.* **2**, 389 (2011).
- [15] Y.-F. Wang, Z.-C. Gu, C.-D. Gong, and D. Sheng, *Phys. Rev. Lett.* **107**, 146803 (2011).
- [16] N. Regnault and B. A. Bernevig, *Phys. Rev. X* **1**, 021014 (2011).
- [17] D. Xiao, W. Zhu, Y. Ran, N. Nagaosa, and S. Okamoto, *Nat. Commun.* **2**, 596 (2011).
- [18] J. W. Venderbos, S. Kourtis, J. van den Brink, and M. Daghofer, *Phys. Rev. Lett.* **108**, 126405 (2012).
- [19] S. Okamoto, N. Mohanta, E. Dagotto, and D. Sheng, *Commun. phys.* **5**, 198 (2022).
- [20] S. Kourtis, T. Neupert, C. Chamon, and C. Mudry, *Phys. Rev. Lett.* **112**, 126806 (2014).
- [21] A. G. Grushin, J. Motruk, M. P. Zaletel, and F. Pollmann, *Phys. Rev. B* **91**, 035136 (2015).
- [22] J. Cai, E. Anderson, C. Wang, X. Zhang, X. Liu, W. Holtzmann, Y. Zhang, F. Fan, T. Taniguchi, K. Watanabe, Y. Ran, T. Cao, L. Fu, D. Xiao, W. Yao, and X. Xu, *Nature* **622**, 63 (2023).
- [23] Y. Zeng, Z. Xia, K. Kang, J. Zhu, P. Knüppel, C. Vaswani, K. Watanabe, T. Taniguchi, K. F. Mak, and J. Shan, *Nature* **622**, 69 (2023).
- [24] H. Park, J. Cai, E. Anderson, Y. Zhang, J. Zhu, X. Liu, C. Wang, W. Holtzmann, C. Hu, Z. Liu, T. Taniguchi, K. Watanabe, J.-H. Chu, T. Cao, L. Fu, W. Yao, C.-Z. Chang, D. Cobden, D. Xiao, and X. Xu, *Nature* **622**, 74 (2023).
- [25] F. Xu, Z. Sun, T. Jia, C. Liu, C. Xu, C. Li, Y. Gu, K. Watanabe, T. Taniguchi, B. Tong, J. Jia, Z. Shi, S. Jiang, Y. Zhang, X. Liu, and T. Li, *Phys. Rev. X* **13**, 031037 (2023).
- [26] Z. Lu, T. Han, Y. Yao, A. P. Reddy, J. Yang, J. Seo, K. Watanabe, T. Taniguchi, L. Fu, and L. Ju, *Nature* **626**, 759 (2024).
- [27] H. Yu, M. Chen, and W. Yao, *Natl. Sci. Rev.* **7**, 12 (2020).
- [28] B. Sutherland, *Phys. Rev. B* **34**, 5208 (1986).
- [29] J. Vidal, R. Mosseri, and B. Douçot, *Phys. Rev. Lett.* **81**, 5888 (1998).
- [30] A. Alexandradinata, T. L. Hughes, and B. A. Bernevig, *Phys. Rev. B* **84**, 195103 (2011).
- [31] R. B. Laughlin, *Phys. Rev. B* **23**, 5632 (1981).
- [32] Q. Niu, D. J. Thouless, and Y.-S. Wu, *Phys. Rev. B* **31**, 3372 (1985).
- [33] H. Li and F. D. M. Haldane, *Phys. Rev. Lett.* **101**, 010504 (2008).
- [34] M. P. Zaletel, R. S. K. Mong, and F. Pollmann, *Phys. Rev. Lett.* **110**, 236801 (2013).
- [35] Z. Guo, X. Lu, B. Xie, and J. Liu, *arXiv preprint arXiv:2311.14368* (2023).
- [36] J. Herzog-Arbeitman, Y. Wang, J. Liu, P. M. Tam, Z. Qi, Y. Jia, D. K. Efetov, O. Vafek, N. Regnault, H. Weng, *et al.*, *arXiv preprint arXiv:2311.12920* (2023).
- [37] J. Dong, T. Wang, T. Wang, T. Soejima, M. P. Zaletel, A. Vishwanath, and D. E. Parker, *arXiv preprint arXiv:2311.05568* (2023).
- [38] Z. Dong, A. S. Patri, and T. Senthil, *arXiv preprint arXiv:2311.03445* (2023).
- [39] N. Morales-Durán, J. Wang, G. R. Schleder, M. Angeli, Z. Zhu, E. Kaxiras, C. Repellin, and J. Cano, *Phys. Rev. Res.* **5**, L032022 (2023).
- [40] N. R. Cooper, *Phys. Rev. Lett.* **106**, 175301 (2011).
- [41] Y. Aharonov and A. Stern, *Phys. Rev. Lett.* **69**, 3593 (1992).
- [42] M. Fishman, S. R. White, and E. M. Stoudenmire, *SciPost Phys. Codebases*, 4 (2022).
- [43] T. D. Kühner, S. R. White, and H. Monien, *Phys. Rev. B* **61**, 12474 (2000).

Supplementary Materials for “Fractional quantum anomalous Hall effect in a semimetal”

Wenqi Yang, Dawei Zhai, Feng-Ren Fan, and Wang Yao*

New Cornerstone Science Laboratory, Department of Physics, University of Hong Kong, Hong Kong, China

ENTANGLEMENT SPECTRUM SCANS ACROSS THE PHASE BOUNDARY

The entanglement spectrum, ϵ_α , is obtained using the relation $\epsilon_\alpha = -\ln(\Lambda_\alpha^2)$ [33], where Λ_α denote Schmidt values obtained from the Schmidt decomposition at the bond connecting left and right halves of the lattice. As shown in Fig. S1, for both entanglement spectrum scans marked by the yellow dashed lines in Fig. 3(c) of the main text, there is a sharp discontinuity at the phase boundary, signaling the transition between the FQAH phase and the metallic phase.

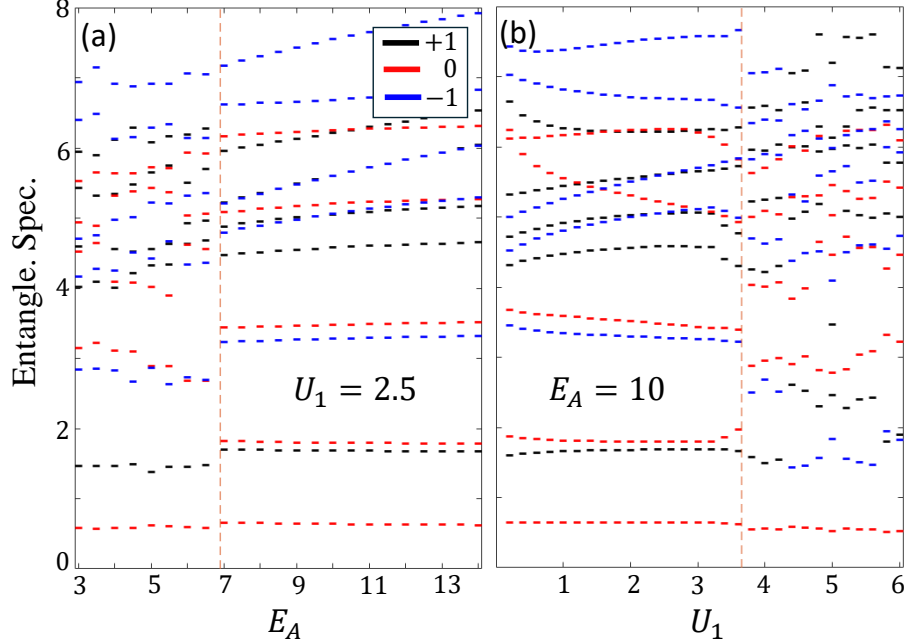


FIG. S1. (a, b) Entanglement spectrum as a function of E_A and U_1 . Different charge sectors are distinguished by different colors [34]. The transition points are marked by the dashed vertical lines where sharp discontinuities of entanglement spectrum can be observed, signaling the transition between the FQAH phase and the metallic phase. $\nu = 5/3$.

EVOLUTION OF THE CHARGE GAP AND PSEUDOSPIN POLARIZATION AT $\nu = 5/3$

The particle-hole excitation gap (charge gap) of the system is given by:

$$\Delta_c = \mu^p - \mu^h. \quad (\text{S1})$$

where μ^p ($-\mu^h$) is the energy of adding a particle (hole) to the system [43]:

$$\begin{aligned} \mu^p &= E^p - E_0 \\ -\mu^h &= E^h - E_0' \end{aligned} \quad (\text{S2})$$

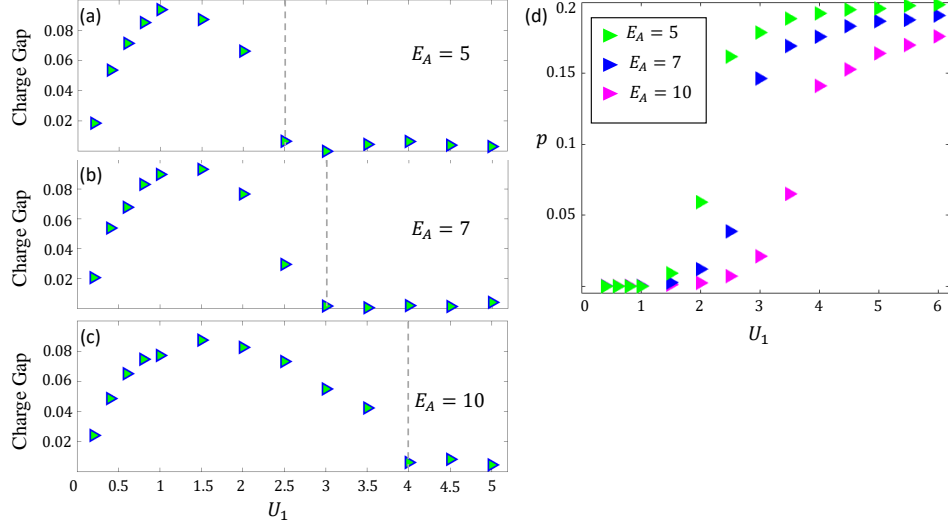


FIG. S2. (a-c) Charge gap as a function of U_1 for different E_A , at $\nu = 5/3$. The dashed vertical lines mark the boundary separating the FQAH and metallic phases. (d) Evolution of pseudospin polarization, $p = \frac{\rho_B - \rho_C}{\rho_B + \rho_C}$, as a function of U_1 , at $\nu = 5/3$.

E_0 here is the ground state energy without the particle and hole, and E^p (E^h) is the total energy of the state with an additional particle (hole), both of which are computed using DMRG calculations.

As shown in Fig. S2 (a)-(c), FQAH phase has a finite charge gap which first increases then decreases as a function of U_1 , reaching zero at the phase boundary and remaining vanishing in the metallic phase. The initial rise in the charge gap can be attributed to the stronger interaction. After a critical U_1 within the FQAH phase, weak pseudospin polarization p spontaneously emerges [Fig. S2 (d)]. A finite p breaks the dark-state symmetry and introduces inhomogeneity to the quantum geometry of the flat band. As a result, the charge gap of the FQAH state decreases. The transition from FQAH to the metallic phase occurs upon a significant increase in p .

PHASE DIAGRAM AT $\nu = 4/3$

The $\nu = 4/3$ phase diagram in the $U_1 - E_A$ parameter space is shown in Fig. S3(a). It consists of the FQAH phase characterized by the fractionally quantized charge pumping, and metallic phase characterized by vanishing charge gap. FQAH phase only exists in a narrow region where U_1 is small. Fig. S3(b) shows examples of the charge pumping simulations of the FQAH phase and metallic phase respectively.

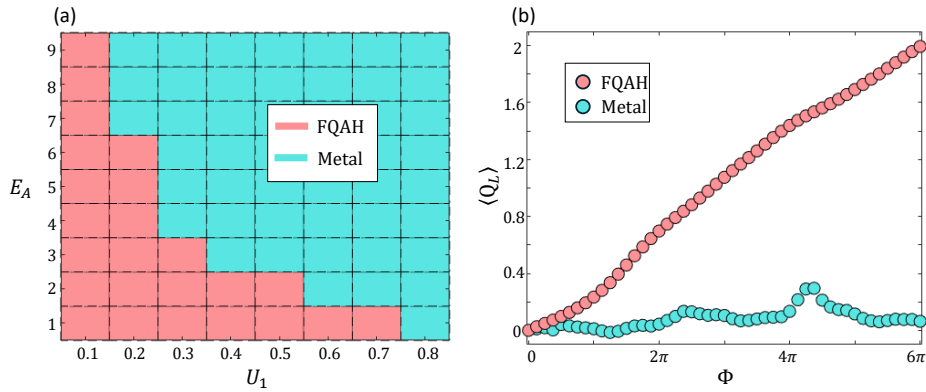


FIG. S3. (a) $U_1 - E_A$ phase diagram at $\nu = 4/3$ filling. (b) Charge pumping simulation results of the FQAH state ($U_1 = 0.1$, $E_A = 7$) and metallic state ($U_1 = 0.5$, $E_A = 8$).